



OPTICAL PROPERTIES OF CERMET MATERIALS

C. Granqvist

► To cite this version:

C. Granqvist. OPTICAL PROPERTIES OF CERMET MATERIALS. Journal de Physique Colloques, 1981, 42 (C1), pp.C1-247-C1-284. 10.1051/jphyscol:1981118 . jpa-00220668

HAL Id: jpa-00220668

<https://hal.science/jpa-00220668>

Submitted on 4 Feb 2008

HAL is a multi-disciplinary open access archive for the deposit and dissemination of scientific research documents, whether they are published or not. The documents may come from teaching and research institutions in France or abroad, or from public or private research centers.

L'archive ouverte pluridisciplinaire **HAL**, est destinée au dépôt et à la diffusion de documents scientifiques de niveau recherche, publiés ou non, émanant des établissements d'enseignement et de recherche français ou étrangers, des laboratoires publics ou privés.

SURFACES SELECTIVES CERMETS.**OPTICAL PROPERTIES OF CERMET MATERIALS**

C.G. Granqvist

Physics Department, Chalmers University of Technology, S-412 96 Gothenburg, Sweden.

Abstract.— Cermets can show a spectral selectivity which makes them well suited for efficient photothermal conversion of solar energy. Sufficiently fine-grained materials can be theoretically understood from effective medium theories. Two formulations apply depending on the microstructure topology ; the Maxwell Garnett theory is valid for metallic particles embedded in an insulating host, whereas the Bruggeman theory holds for a random mixture of metallic and insulating particles. We discuss extensions to treat size dependent electron scattering, shape and orientation effects, and the role of local aggregation. The theories are applied to several types of cermets : discontinuous metal films, gas evaporated coatings, coevaporated and cosputtered layers, electrodeposited films, and electrolytically and integrally coloured anodic aluminium oxide coatings. Successes and failures of the theoretical models are discussed and remaining uncertainties are pointed out. One general conclusion is that effective medium theories are very useful for understanding the optical properties both qualitatively and quantitatively. Another general result is that lack of sufficiently accurate sample characterization is still hampering further progress for several types of technologically interesting cermets.

1. **Introduction.**— Cermets are fine-grained mixtures of metallic and insulating components. The optical properties of such materials have been studied for many years, but their importance for selective absorption of solar energy has led to a greatly increased interest recently /1/. This paper discusses results for several different kinds of metal-insulator mixtures. Some of these are "model systems", being laboratory analogues of practically useful materials, whereas others are fully developed solar absorbers. The paper is not a complete review of the field but rather a number of selected examples. Most of these are connected with work carried out at Chalmers University of Technology.

Figure 1 provides a starting point for discussing selective absorption of solar energy. The solid curve in part (b) shows a typical solar spectrum, which is seen to be confined to the wavelength interval $0.3 \leq \lambda \leq 2 \mu\text{m}$. The dashed curves to the right represent the emitted black-body radiation for surfaces at the stated temperatures. The negligible over-

lap between the solar and thermal spectra makes it possible to design surfaces capable of absorbing most of the solar radiation by having low reflectance at $\lambda \lesssim 2 \mu\text{m}$ while at the same time minimizing radiative losses by having low emissivity, i.e., high reflectance, at $\lambda \gtrsim 2 \mu\text{m}$ /2,3/. The desired steplike reflectance profile can be obtained by applying films which absorb at $\lambda \lesssim 2 \mu\text{m}$ but are transparent elsewhere onto highly conducting substrates. Several different types of such coatings are conceivable ; the most useful ones seem to be comprised of cermets. Two examples are shown in figure 1a. The dotted curve stems from coevaporated Ni and Al_2O_3 deposited onto silver. The data are taken from the work by Craighead and Buhrman /4/. Similar results have been reported also by others /5,6/. The solid curve, which practically overlaps the dotted one, was obtained for our Ni pigmented anodic Al_2O_3 films /7/ to be discussed in more detail later in this paper. The latter type of coatings are presently being used on flat-plate collectors for photothermal conversion of solar energy.

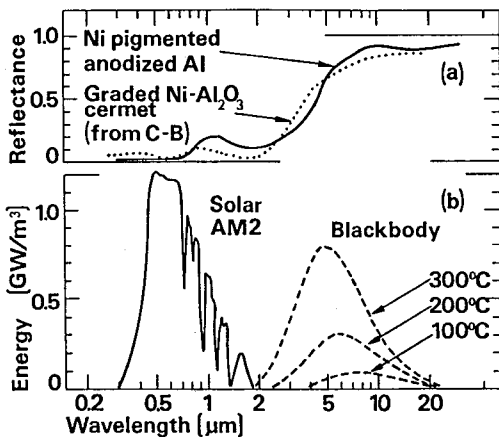


Fig.1 - Part (a) shows a typical spectral reflectance curve for the Ni pigmented anodized Al surfaces to be discussed below, together with a curve for a coevaporated Ni-Al₂O₃ cermet as taken from a report by Craighead and Buhrman (C-B). The solid curve in part (b) depicts the solar spectrum AM2 referring to typical clear weather conditions and the sun standing 30° above the horizon. The dashed curves show blackbody radiation spectra for three temperatures.

The optical properties of the cermets can be treated in terms of effective medium theories, as discussed in section 2. The basic formulations outlined there are then applied to a number of metal-insulator systems,

starting from the simpler and less applied ones and going towards more complex but also more practically useful systems. We cover briefly discontinuous gold films (Sec. 3), gas evaporated coatings of various metals (Sec. 4), codeposited films (Sec. 5), electrodeposited layers (Sec. 6), and electrolytically and integrally coloured anodic Al_2O_3 films on Al sheet (Sec. 7). The paper is concluded in section 8 by a summary and some remarks.

2. Outline of effective medium theories. - The metallic particles in the cermets are normally very small. The cermets are also fairly homogeneous on the scale of the relevant light wavelengths. These facts make effective medium theories applicable. Two different types of theories have become popular ; these are usually ascribed to J.C.M. Garnett /8/ (known as "the Maxwell Garnett theory") and to D.A.G. Bruggeman /9/. The theories can be obtained from a unified conceptual framework by considering the scattering from properly defined random unit cells. For the Maxwell Garnett (MG) theory, this is the metallic sphere surrounded by a concentric insulator shell. The relative volumes of the two components correspond to the overall volume fraction in the two-phase cermet /10-12/. Requiring now that first order scattering off this unit cell shall vanish gives the wellknown equation

$$\frac{\bar{\epsilon}^{\text{MG}} - \epsilon_m}{\bar{\epsilon}^{\text{MG}} + 2\epsilon_m} = f \frac{\epsilon - \epsilon_m}{\epsilon + 2\epsilon_m}, \quad (1)$$

where $\bar{\epsilon}^{\text{MG}}$ is the average dielectric permeability, ϵ is the dielectric permeability of the metallic particles, ϵ_m refers to the insulating medium, and f is the volume fraction occupied by particles (the "filling factor"). The Bruggeman (Br) theory can be obtained analogously from a random unit cell being a single sphere which has a probability f of being metallic and a probability $1-f$ of being insulating. Requiring, again, that first order scattering shall vanish /13,14/ leads to

$$f \frac{\epsilon - \bar{\epsilon}^{\text{Br}}}{\epsilon + 2\bar{\epsilon}^{\text{Br}}} + (1-f) \frac{\epsilon_m - \bar{\epsilon}^{\text{Br}}}{\epsilon_m + 2\bar{\epsilon}^{\text{Br}}} = 0 \quad (2)$$

Neither the Maxwell Garnett nor the Bruggeman theories, derived according to the above schemes, are confined to small filling factor. It is important to note, though, that equations (1) and (2) pertain to totally different microstructures : the Maxwell Garnett theory holds for particles in a continuous host, while the Bruggeman theory applies to a random mixture of conducting and insulating spheres. Therefore only

the Bruggeman formalism predicts a percolation threshold. The scattering approach is also suitable for assessing higher order corrections to the two effective medium theories.

Equations (1) and (2) are often too simple to be directly applicable to experimental samples, which may be characterized by size dependent dielectric permeabilities, non-spherical particle shapes, preferred orientation of elongated grains, and strong aggregation effects. All of these can be incorporated to some extent in the effective medium theories -at least when the filling factor is not too large- by a largely intuitive reasoning. To this end we rewrite the above equations to read

$$\frac{\epsilon_{MG}}{\epsilon_m} = \frac{1 + \frac{2}{3} f\alpha}{1 - \frac{1}{3} f\alpha} \quad (3)$$

$$\alpha = \frac{\epsilon - \epsilon_m}{\epsilon_m + \frac{1}{3} (\epsilon - \epsilon_m)} \quad (4)$$

$$\text{and } \frac{\epsilon_{Br}}{\epsilon_m} = \frac{1 - f + \frac{1}{3} f\alpha'}{1 - f - \frac{2}{3} f\alpha'} \quad (5)$$

$$\alpha' = \frac{\epsilon - \bar{\epsilon}_{Br}}{\bar{\epsilon}_{Br} + \frac{1}{3} (\epsilon - \bar{\epsilon}_{Br})} \quad (6)$$

The self-consistent nature of the Bruggeman theory is apparent. It is also observed that α is proportional to the polarizability of a sphere (whose depolarization factor is $\frac{1}{3}$).

A size dependence in the dielectric permeability of the particles can be accounted for by the substitutions $\epsilon \rightarrow \epsilon_j$, $\alpha \rightarrow \alpha_j$, $f\alpha \rightarrow \sum_j f_j \alpha_j$ and similarly for α' . The subscript denotes particles belonging to the j^{th} column in a size histogram (centred at diameter x_j) and the f_j 's are fractional filling factors normalized by $\sum_j f_j = f$. The size dependence now enters via ϵ_j , which is composed of contributions from free electrons (Drude theory) and from bound electrons. The latter relate to the bandstructure, which is not expected to change much in particles with diameters larger than, say, 3 nm. The Drude part, though, contains an electron lifetime which is a direct measure of the mean free path between scattering events. An altered scattering time can be incorporated by writing

$$\epsilon_j(\omega) = \epsilon_{\text{expt}}(\omega) - \epsilon_{\text{expt}}^{\text{Drude}}(\omega) + \epsilon_j^{\text{Drude}}(\omega) \quad (7)$$

$$\epsilon_{\text{expt}}^{\text{Drude}}(\omega) = 1 - \frac{\omega_p^2}{\omega(\omega+i/\tau_b)} \quad (8)$$

$$\epsilon_j^{\text{Drude}}(\omega) = 1 - \frac{\omega_p^2}{\omega(\omega+i/\tau_j)} \quad (9)$$

where $\epsilon_{\text{expt}}(\omega)$ is the experimentally determined dielectric function for the bulk material, $\hbar\omega$ is the photon energy, $\hbar\omega_p$ is the plasma energy, τ_b is the mean lifetime for bulk scattering, and τ_j is the mean lifetime for scattering of electrons in the fine particles. τ_j can be expressed as

$$\tau_j^{-1} = \tau_b^{-1} + v_F/l_j, \quad (10)$$

where v_F is the Fermi velocity, and l_j is the mean free path, which, in its turn, depends on the type of scattering. If diffuse boundary scattering is dominating one can show that $1/15/l_j = x_j/2$, whereas a shorter distance is valid if defect scattering is important /16/. Thus the dielectric permeability of the particles is related to the size distribution, which often can be accurately, represented by a log-normal curve /17/. This is governed by two parameters, the median size and the geometric standard deviation, both of which can be obtained by plotting the cumulative distribution on log-probability paper /17/.

Non-spherical particle shapes can be treated by replacing the expressions for α_j and α'_j by others which relate to the polarizability of the actual shape. A general expression for ellipsoidal grains is /18/

$$\alpha_j = q \sum_i \frac{\epsilon_j - \epsilon_m}{\epsilon_m + L_j^{(i)} (\epsilon_j - \epsilon_m)}, \quad (11)$$

and analogously for α'_j . Here $L_j^{(i)}$ denotes the appropriate depolarization factors and q takes on different values depending on the orientation of the particles. Simple expressions are valid for spheroids. These are specified by the axes $a_j > b_j > c_j$. With the convention that $L_j^{(1)} \leq L_j^{(2)} \leq L_j^{(3)}$, we find for prolate (P) and oblate (O) spher-

Table I.- Parameters q and $L_j^{(i)}$ in equation (11) for different shapes and orientations of spheroidal particles.

Shape	Orientation	q	$L_j^{(i)}$
Sphere	-	1	$\frac{1}{3}$
Prolate spheroid	Random	$\frac{1}{3}$	$L_{jP}^{(1)}; L_{jP}^{(2)}; L_{jP}^{(3)}$
	$a_j \parallel$ surface, otherwise random	$\frac{1}{2}$	$L_{jP}^{(1)}; L_{jP}^{(2)}$
	$a_j \perp$ surface	1	$L_{jP}^{(3)}$
Oblate spheroid	Random	$\frac{1}{3}$	$L_{jO}^{(1)}; L_{jO}^{(2)}; L_{jO}^{(3)}$
	$c_j \parallel$ surface, otherwise random	$\frac{1}{2}$	$L_{jO}^{(2)}; L_{jO}^{(3)}$
	$c_j \perp$ surface	1	$L_{jO}^{(1)}$

roids and normally incident light the quantities listed in table I, where the depolarization factors are given by /19/

$$L_{jP}^{(1)} = (e_{jP}^{-3} - e_{jP}^{-1}) \left\{ \frac{1}{2} \ln \left[(1+e_{jP})/(1-e_{jP}) \right] - e_{jP} \right\}, \quad (12)$$

$$L_{jP}^{(2)} = L_{jP}^{(3)} = \frac{1}{2} (1 - L_{jP}^{(1)}), \quad (13)$$

$$e_{jP} = (1 - c_j^2/a_j^2)^{1/2}, \quad (14)$$

and

$$L_{jO}^{(3)} = (e_{jO}^{-3} + e_{jO}^{-1}) (e_{jO} - \arctan e_{jO}), \quad (15)$$

$$L_{jO}^{(1)} = L_{jO}^{(2)} = \frac{1}{2} (1 - L_{jO}^{(3)}), \quad (16)$$

$$e_{jO} = (a_j^2/c_j^2 - 1)^{1/2}. \quad (17)$$

The cube-shaped particle can be described by /20/

$$\alpha_j = \sum_i \frac{C_i (\epsilon_j - \epsilon_m)}{\epsilon_m + L_c^{(i)} (\epsilon_j - \epsilon_m)}, \quad (18)$$

where only six pairs of C_i and $L_c^{(i)}$ need to be considered. These numbers are listed in table II.

Table II.- Parameters C_i and $L_c^{(i)}$ in equation (18) for cube-shaped particles.

i	C_i	$L_c^{(i)}$
1	0.44	0.214
2	0.24	0.297
3	0.04	0.345
4	0.05	0.440
5	0.10	0.563
6	0.09	0.706

It is of interest to study also non-homogeneous particles. For spherical metallic shells surrounding a core with dielectric permeability ϵ_c one obtains /21/

$$\alpha_j = 3 \frac{(\epsilon_j - \epsilon_m)(\epsilon_c + 2\epsilon_j) + \Omega_j (2\epsilon_j + \epsilon_m)(\epsilon_c - \epsilon_j)}{(\epsilon_j + 2\epsilon_m)(\epsilon_c + 2\epsilon_j) + \Omega_j (2\epsilon_j - 2\epsilon_m)(\epsilon_c - \epsilon_j)}, \quad (19)$$

where Ω_j is the ratio between the volumes of the outer and inner sphere for size j. Metallic cores surrounded by a dielectric shell can be treated by making the replacements $\epsilon_j \rightarrow \epsilon_c$ and $\epsilon_c \rightarrow \epsilon_j$. It is possible to make computations also for confocal spheroids. For metallic cores and random orientation one can show that /22, 23/

$$\alpha_j = \frac{1}{3} \sum_{i=1}^3 \frac{(\epsilon_c - \epsilon_m) \left[\epsilon_c + (\epsilon_j - \epsilon_c) (L_j^{(i)in} - \Omega_j L_j^{(i)out}) \right] + \Omega_j \epsilon_c (\epsilon_j - \epsilon_c)}{\left[\epsilon_c + (\epsilon_j - \epsilon_c) (L_j^{(i)in} - \Omega_j L_j^{(i)out}) \right]} x \\ x = \frac{1}{\left[\epsilon_m^{-L_j^{(i)out}} (\epsilon_m - \epsilon_j) \right] + \Omega_j L_j^{(i)out} \epsilon_c (\epsilon_j - \epsilon_c)}, \quad (20)$$

where $L_j^{(i)in}$ and $L_j^{(i)out}$ refer to the inner and outer spheroid. Other orientations can be treated in analogy with the results in table I. Pronounced aggregation of spherical particles is found experimentally particularly for gas evaporated samples. Local field effects, which are strong within the clusters, can be accounted for approximately by using results by Clippe et al. /24/ who considered non-retarded dipole-dipole coupling among certain geometrically well defined aggregates. Their results can be obtained by replacing the geometrical depolarization factor by a triplet of effective depolarization factors $L^{(i)*}$ in the expression for α_j . This quantity should then be written /25/

$$\alpha_j = \frac{1}{3} \sum_{i=1}^3 \frac{\epsilon_j - \epsilon_m}{\epsilon_m + L^{(i)*} (\epsilon_j - \epsilon_m)} . \quad (21)$$

The pertinent values of the effective depolarization factors are found in table III for a number of interesting aggregates.

Table III.- Effective depolarization factors in equation (21) for several geometrical configurations of aggregated spheres.

Geometrical configuration	Equivalent depolarization factor $L^{(1)*}$	Equivalent depolarization factor $L^{(2)*}$	Equivalent depolarization factor $L^{(3)*}$
Single sphere	$\frac{1}{3}$	$\frac{1}{3}$	$\frac{1}{3}$
Double sphere	0.250	0.375	0.375
Single strand chain	0.133	0.435	0.435
Double strand chain	0.139	0.342	0.518
fcc lattice	0.0865	0.0865	0.827

3. Discontinuous films.- Extremely thin layers of metal deposited onto non-conducting substrates are not continuous but consist of discrete islands. The optical properties of such discontinuous films are qualitatively different from those of the continuous layers as illustrated in figure 2. The solid curve shows a transmittance spectrum measured for a discontinuous gold film with average thickness 3.0 nm. A minimum is found at $\lambda \approx 0.65 \mu\text{m}$. A thicker continuous film, on the other hand, yields that the transmittance is enhanced as one goes towards shorter wavelengths, which is expected from the Drude theory, until interband absorption cuts down the transmittance at $\lambda \lesssim 0.5 \mu\text{m}$. For comparison, figure 2 contains a curve for gas evaporated gold particles also ; this

resembles the one for discontinuous films. Thus the discontinuous films can display some spectral selectivity, with absorptance at short wavelengths and transmittance at longer wavelengths, which motivates that such films are regarded in connection with solar absorbing materials. The selectivity is not strong enough for practical applications in the case of the single discontinuous films but multilayer deposits, such as those discussed by Zeller and Kuse, /26/ can exhibit excellent optical properties. However, the complex fabrication excludes large scale applications.

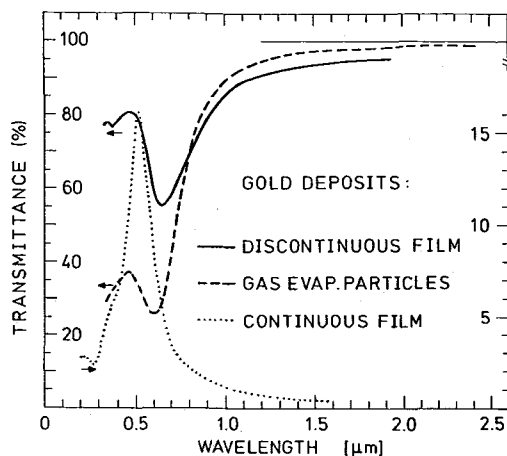


Fig.2.- Measured spectral transmittance for normal incidence onto gold deposits prepared in three different ways. Data are shown for a discontinuous film (average thickness 3.0 nm), gas evaporated particles, and for a continuous film (thickness 48 nm). Note the different vertical scales for the curves, as indicated by the arrows.

Our discontinuous gold films /27/ were produced by evaporation from a resistively heated source onto Corning 7059 substrates under ultrahigh vacuum conditions while maintaining an electric field of 20 V/cm in the substrate plane. The substrate was kept at room temperature. The amount of material impinging towards the substrate was determined via a calibrated quartz crystal oscillator microbalance, whose reading was converted to an effective thickness t for an ideal continuous film with bulk density. After aging in vacuum for more than 20 h, the films were transferred to a spectrophotometer and their transmittance was measured. Subsequently, an amorphous carbon layer was deposited on top of the gold, the glass was dissolved in HF acid, and the free films were analysed by transmission electron microscopy.

Electron micrographs for discontinuous films with four different mass

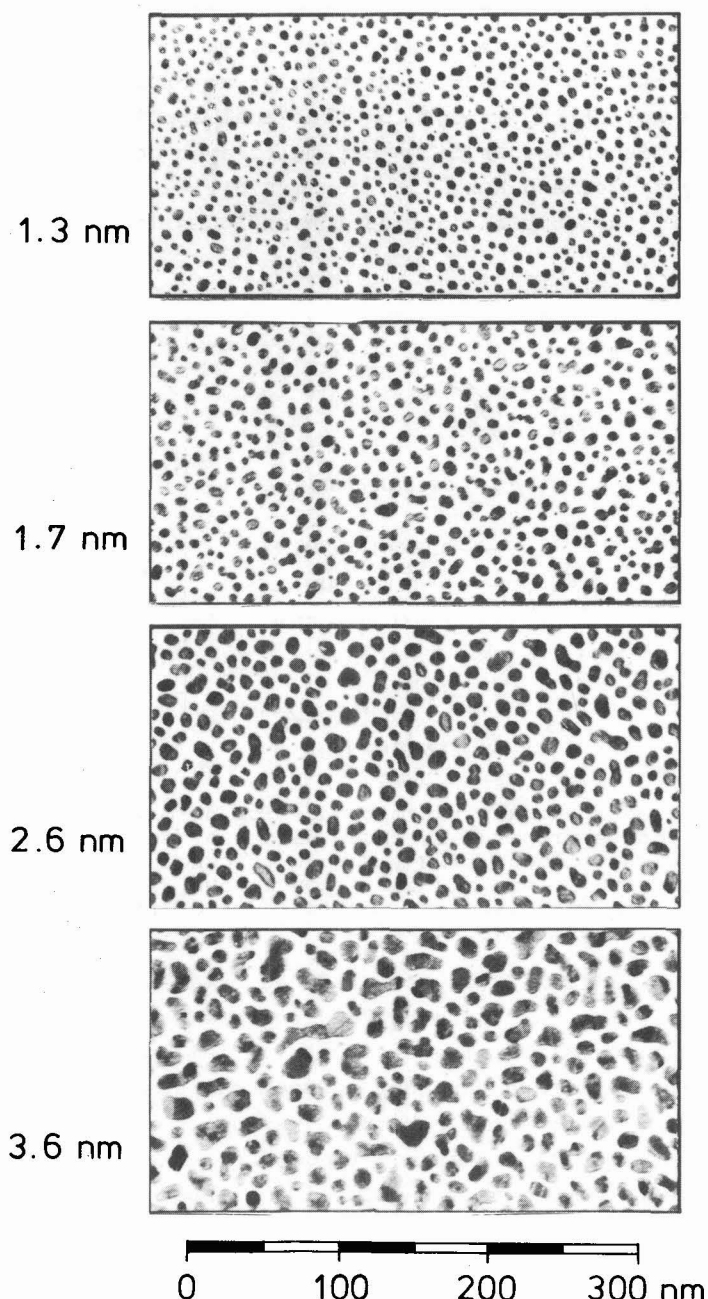


Fig.3.- Transmission electron micrographs for discontinuous gold films with four mass thicknesses.

thicknesses are shown in figure 3. When t is increased the average size of the islands as well as their irregularity is enhanced. The two-dimensional images of the islands can be represented by ellipses whose axes, empirically, obey log-normal distributions. Combining these data with the measured number density of islands shows that an accurate model of the three-dimensional shape of the islands is given by prolate spheroids with symmetry axis along the substrate plane. Thus the electron microscope data can be used to evaluate depolarization factors for the islands. The final parameter needed is a mean interisland separation D which is obtained -somewhat arbitrarily- by determining for each island the distances to its four nearest neighbours and associating an average island-to-island separation with the arithmetic mean of these lengths. The mode in the distribution of such average lengths is taken to be the mean interisland separation of the entire film.

Figure 4 shows measured spectral transmittance for discontinuous gold films with several mass thicknesses. The most salient feature is a minimum occurring at 0.56 to 0.70 μm . The minimum shifts towards larger wavelengths in the thicker films at the same time as the spectral selectivity is being gradually lost.

It has been shown convincingly by Bedaux and Vliegler /28/ that the Maxwell Garnett approach is adequate for a theoretical treatment of the optical properties of discontinuous films, provided that an "optical" thickness is invoked properly. A relation /28/

$$t_{\text{opt}} = \frac{4}{3} \langle \Lambda \rangle \quad (22)$$

is appropriate, where $\langle \Lambda \rangle$ is related to an average distance between the islands. The prefactor is valid for an "amorphous" distribution of islands while somewhat different factors are obtained under other conditions. The filling factor is given by :

$$f = t/t_{\text{opt}} \quad (23)$$

We computed optical data by use of empirical results for particle sizes, shapes, and mean separations ($\langle \Lambda \rangle = D$) ; ϵ_{expt} was obtained from Winsemius's data /29/, from which we extracted $\hbar\omega_p = 8.55 \text{ eV}$, $\hbar/\tau_b = 0.108 \text{ eV}$, and $v_F/c = 4.7 \times 10^{-3}$. Consistently, the computed transmittance was much larger than the measured one. The discrepancy cannot be ascribed to uncertainties in the determinations of particle size and shape, to substrate interaction, or to the formation of dielectric pellicles /27/.

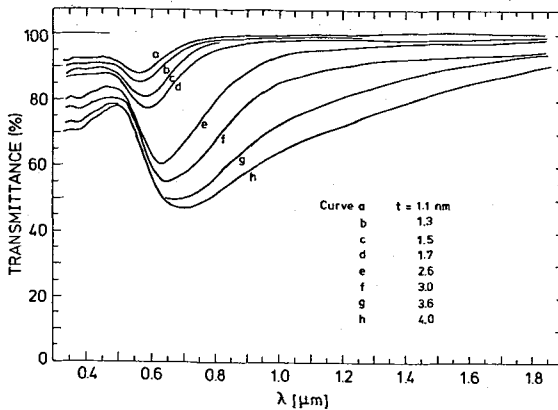


Fig.4.- Spectral transmittance for discontinuous gold films with eight mass thicknesses.

However, a reconciliation of theory and experiments can be achieved if the role of $\langle A \rangle$ is considered in more detail. It can be shown that this quantity must be weighted strongly in favour of the smallest particle separations. Therefore we introduce a fitting parameter ξ_{fit} by

$$t'_{\text{opt}} = \frac{4}{3} \xi_{\text{fit}}^D. \quad (24)$$

This sole parameter was varied to arrive at the final comparison of theory and experiments shown in figure 5. We used $\epsilon_m = 1.2 + i 0.12$ to allow for some interaction with the substrate as well as a weak tunnelling conductivity between the islands. The pertinent values of ξ_{fit} are given in figure 6 together with results for $f_{\text{fit}} = t/t'_{\text{opt}}$. The agreement between theory and experiments is seen to be excellent for $t \lesssim 3$ nm, while the computed minima are too narrow for larger mass thicknesses. This is not an unexpected result, since in these films the islands look rather irregular so that the spheroidal approximation may break down. The main conclusion is that the optical properties of two-dimensional particulate films can be reproduced quantitatively from an effective medium theory. The weak spectral selectivity in the measured data can thus be theoretically understood.

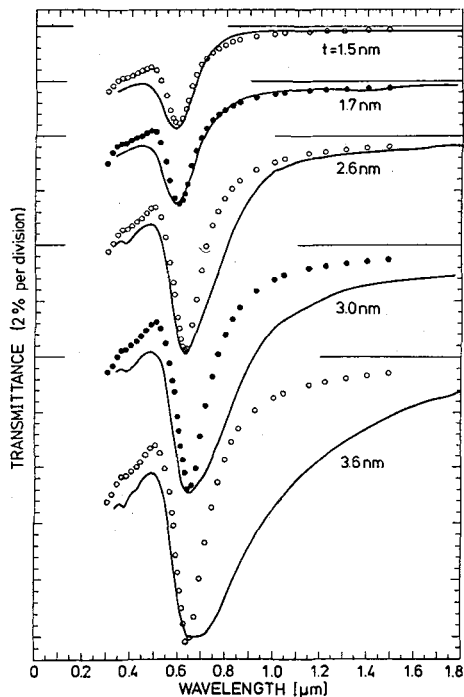


Fig.5.- Spectral transmittance for five discontinuous gold films. Solid curves denote measurements and circles denote computations using the ξ 's fit of figure 6.

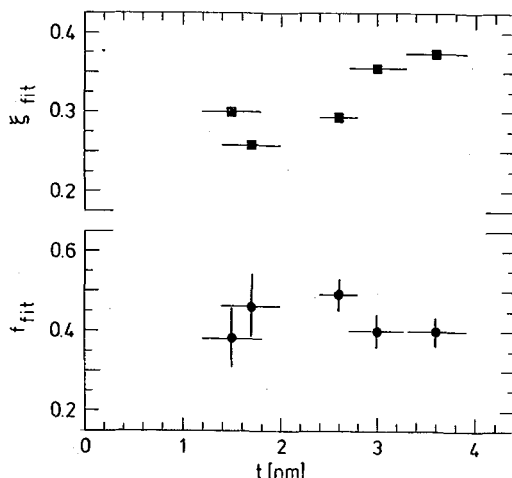


Fig.6.- Values of ξ_{fit} and f_{fit} for discontinuous gold films with different thicknesses.

4. Gas evaporated particles.- Films comprised of gas evaporated particles represent the next step towards a practically useful absorber of solar energy. These surfaces can show the desired optical properties but, unfortunately, they lack sufficient mechanical rigidity. Nevertheless, gas evaporated films are convenient as model substances, which simulate the properties of a practical coating, their main virtue being the easy fabrication technique and the straightforward sample analysis. Below we discuss gas evaporated particles of gold /25/, aluminium /30/, chrome /31/, and nickel /32/.

The gold particles /25/ were prepared by evaporation from a tungsten boat in a conventional bell jar evaporator containing 2 torr of air. The metal atoms, which are effused from the vapour source, lose their energy rapidly through collisions with the gas atoms, so that a highly supersaturated state is reached from which stable clusters of metal atoms are produced by homogeneous nucleation. These embryonic particles then grow by liquid-like coalescence to form larger grains whose ultimate size is governed by experimental conditions such as evaporation rate, atomic or molecular weight of the gas, its pressure etc. The presence of oxygen makes the particles electrically decoupled presumably by oxide formation. Soot-like particle films were collected onto glass substrates. Their thickness t was determined by optical microscopy and their mass per unit area (W/A) by weighings. The filling factor was then obtained from

$$f = (W/A) (\rho t)^{-1}, \quad (25)$$

where ρ is the density of bulk gold. Electron microscope grids covered with amorphous carbon layers were placed close to the substrates and exposed to the particles simultaneously with the glass plates. Figure 7a shows a transmission electron micrograph. Spherical particles with average size around 3 nm are seen. These form complex chains and clusters. Such clumping is characteristic for gas evaporated specimens. Figure 7b reproduces an electron diffraction image of the same sample. Its main constituent is found to be fcc Au. One faint ring can presumably be ascribed to volatile tungsten trioxide.

Optical transmittance for normal incidence was recorded in the interval $0.3 < \lambda < 2.5 \mu\text{m}$. Figure 8 shows spectral data for four samples with different masses per unit area. The most noteworthy feature is the dip in the transmittance at a wavelength of 0.56 to 0.60 μm . Clearly, the spectral selectivity inherent in these curves is in qualitative agreement with that for discontinuous gold films.

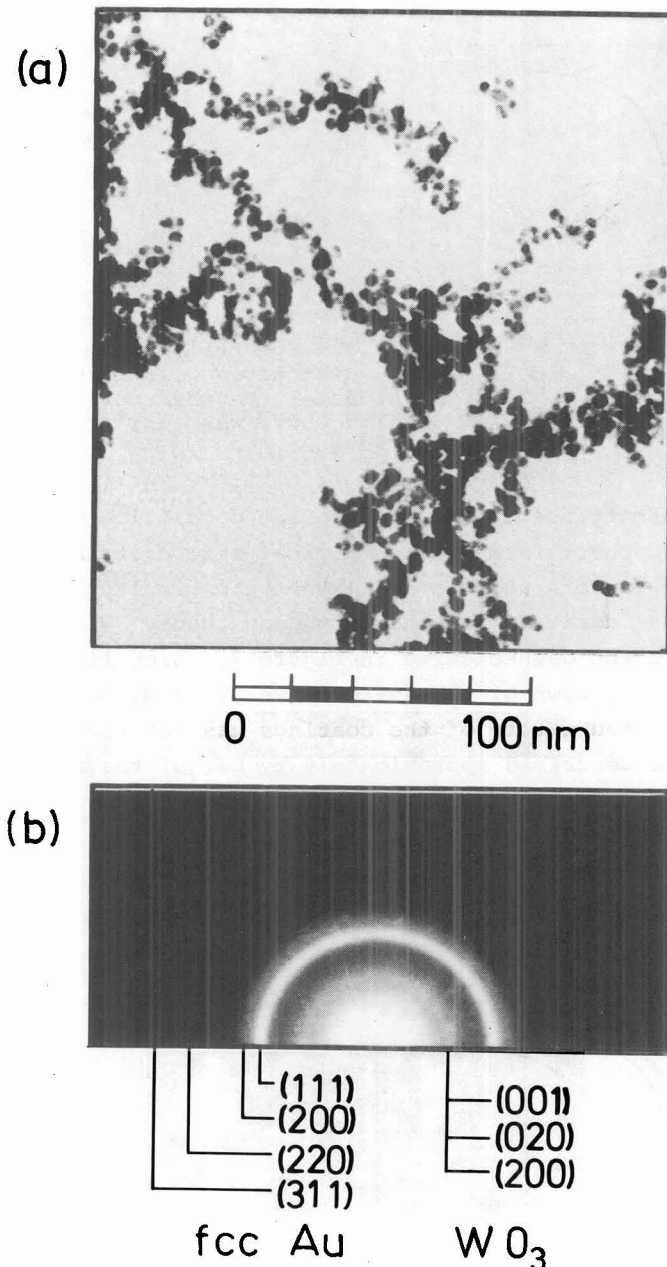


Fig.7.- Part (a) shows a transmission electron micrograph for gas evaporated gold particles. Part (b) depicts an electron diffractogram of the same sample. Calculated positions for the reflections from fcc gold and from triclinic or orthorhombic WO₃ are indicated.

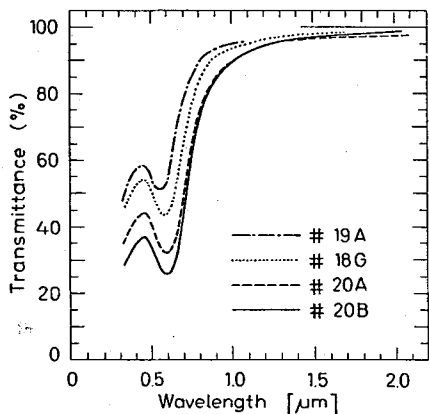


Fig.8.- Spectral transmittance for gas evaporated gold films with four values of the mass per unit area. The solid curve was earlier shown in figure 2.

The spectral transmittance of the particulate gold films was calculated from the Maxwell Garnett formalism. Empirical size distributions were used. The filling factors were so small that the results do not deviate markedly from those derived from the Bruggeman theory. With no free parameters we obtain the dashed curve in figure 9, which lies much above the measured spectrum shown by the solid curve. This difference occurs because the aggregated nature of the coatings has not been included. This effect can be described approximately by use of the fictitious depolarization factors listed in table III. Assuming aggregates being double spheres, chains, and closepacked clusters yields progressively lower spectral transmittance, as shown in figure 9. The dash-dotted curve pertaining to chains is found to correspond rather well with the measurements.

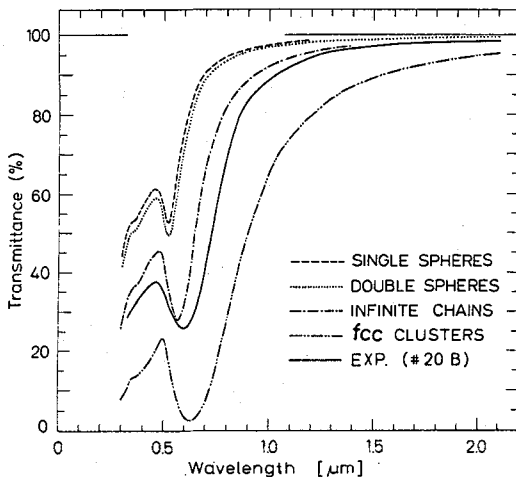


Fig.9.- Spectral transmittance for gold particles with different types of aggregation.

To obtain a final comparison of theory and experiments we considered the sample to be a mixture of aggregates of spheres with several well-defined configurations. Specifically, we chose independent spheres, linear chains, and fcc clusters. These types of structures were documented by the electron micrographs. We hence required that the filling factor would be

$$\begin{aligned}\xi f &\quad \text{for independent spheres,} \\ \zeta f &\quad \text{for chains,} \\ (1-\xi-\zeta)f &\quad \text{for fcc clusters,}\end{aligned}$$

where ξ , $\zeta \geq 0$ and $\xi + \zeta \leq 1$. Neither ξ nor ζ needs to represent exactly the "true" fractions of independent particles or chains, because we have not attempted to include any relative absorption strength for the different aggregates. Figure 10 shows calculated and measured transmittance spectra for two samples. With the shown percentages of the three kinds of aggregates, it is evident that one can bring the computations into very good agreement with the measurements over the whole spectral range. This indicates that the optical properties of gas evaporated films can be quantitatively understood from the sizes of the particles and their aggregation.

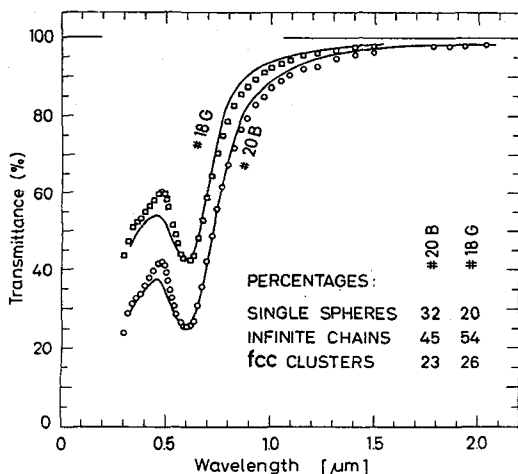


Fig.10.- Spectral transmittance for two films consisting of gas evaporated gold particles. Solid curves denote experimental data. Squares and circles represent calculations applying to the shown kinds of aggregation.

Ultrafine aluminium particles /30/ are of interest in connection with integrally coloured anodic Al_2O_3 films /33, 34/ which have potential interest for selective absorption of solar energy /35/. We prepared such particles by evaporation in 3 torr of He gas to which a small amount of O_2 was introduced continuously. Particles with mean diameters of 3 to 4 nm were formed. Transmittance spectra for two coatings are shown by

the solid curves in figure 11.

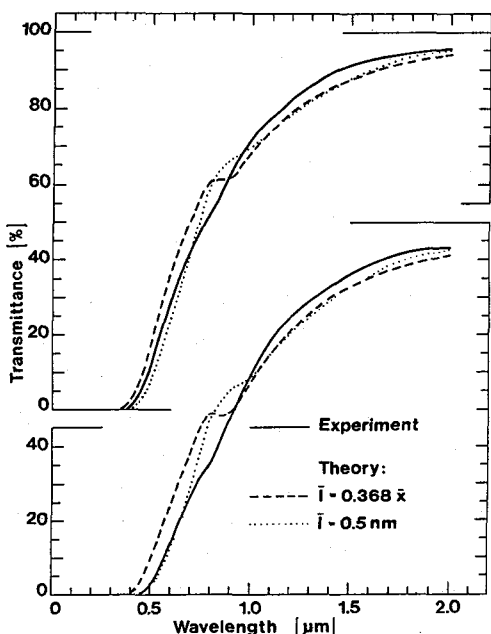


Fig.11.- Spectral transmittance for two films consisting of gas evaporated aluminium particles. Solid curves denote experimental data. Dashed and dotted curves represent calculations applying to two different types of electron scattering.

Strong spectral selectivity is apparent. To understand this effect, we employed the Maxwell Garnett formalism. The oxide coated Al grains were characterized by /36/ $\hbar\omega_p = 15.2$ eV, $\hbar/\tau_b = 0.065$ eV, empirical mass per unit area and size distribution, the same aggregation as found for the Au grains, $\epsilon_c = 3$, and $\Omega = 0.4$. The latter result for the oxide content is consistent with electron microscopic evidence. Assuming boundary scattering of the conduction electrons (i.e., a median mean free path given by $\bar{\lambda} = 0.368 \bar{x}$, where \bar{x} is the median diameter) gives the dashed curves in figure 11. The structure at $\lambda \approx 0.85 \mu\text{m}$, which is caused by parallel band absorption /37/, is much stronger than in the spectrophotometric data. This can be understood -at least partially- if the mean free path is very short, and the dotted curves referring to $\bar{\lambda} = 0.5 \text{ nm}$ agree rather well with the measurements. It should be noted that the computed wavelength of the parallel band absorption is insensitive to the parameters of our theoretical model.

Ultrafine particles of chrome and nickel are of particular interest, since these are responsible for the spectral selectivity in several types of practical absorber surfaces. Chrome particles /31/ were made by evaporation in 2.5 torr of argon and 0.1 torr of air onto infrared transparent KBr plates. Transmittance data are shown in figure 12 for films

with six different values of W/A. The thicker deposits have the desired optical properties with high absorptance over the solar spectrum and high transmittance in the thermal range. The absorption band at $16 \lesssim \lambda \lesssim 19 \mu\text{m}$ is caused by Cr_2O_3 pellicles. Computations based on published /38, 39/ bulk data for chrome gave results such as those shown in figure 13 for different kinds of aggregation. Just as for the Au particles, best agreement between theory and experiments is observed when linear chains of spheres are considered.

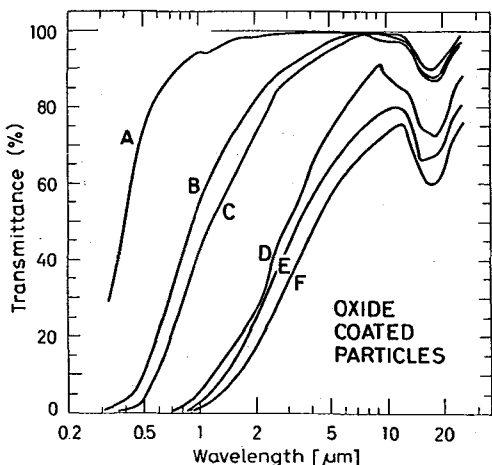


Fig.12.- Spectral transmittance for gas evaporated chrome films with six different values of the mass per unit area.

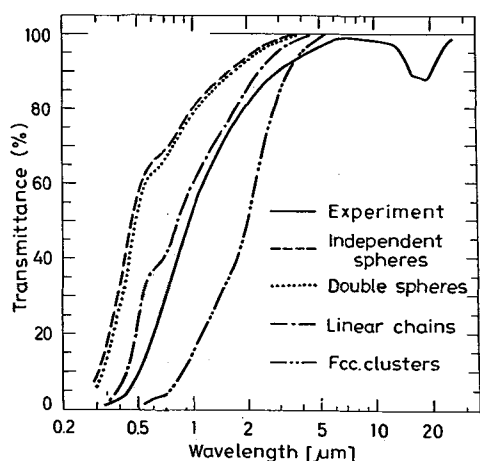


Fig.13.- Spectral transmittance for a film consisting of gas evaporated chrome particles. Solid curve denotes experimental data. Dashed and dotted curves represent calculations applying to the shown kinds of aggregation.

Nickel particles /32/ were produced by evaporation in 2 torr of argon onto KBr substrates. Subsequent heatings for 3 minutes at 400°C gave electrical decoupling of the individual grains. Reproducible spectral

transmittance was recorded, as shown by figure 14.

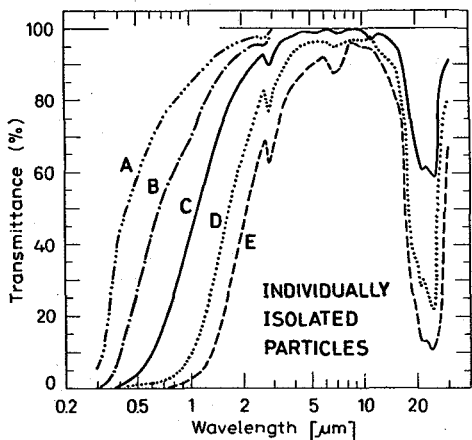


Fig.14.- Spectral transmittance for gas evaporated nickel films with five different values of the mass per unit area.

The strong minima at $20 \lesssim \lambda \lesssim 25 \mu\text{m}$ are caused by NiO. Heat treatments up to 600°C affected the spectra only marginally, which is seen from figure 15. Gas evaporated chrome particles, on the other hand, deteriorate already at 300°C . This implies that surfaces with Ni grains are inherently more stable against thermal degradation than those based on Cr grains. The optical data can be quantitatively explained in exactly the same way as already discussed for Au, Al, and Cr particles.

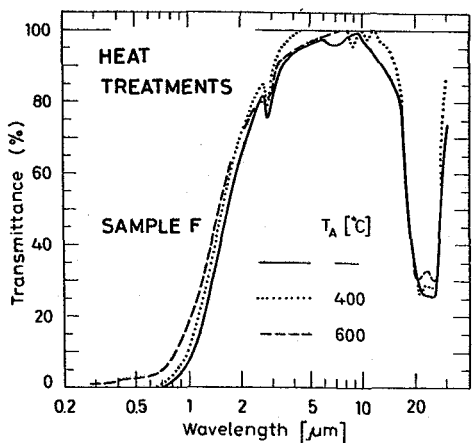


Fig.15.- Spectral transmittance for a gas evaporated nickel film after annealing for more than 20 h at the shown temperatures.

Summarizing, gas evaporated metal particles can exhibit a spectral selectivity which make them well suited for efficient photothermal conversion of solar energy. The optical data can be quantitatively understood from the Maxwell Garnett theory provided that the aggregated nature of

the specimens is accounted for properly. The lack of mechanical stability puts severe restrictions on practical use, though.

5. Codeposited films.- The lack of sufficient ruggedness, which characterizes the gas evaporated films, can be avoided by simultaneous deposition of metal and insulator onto substrates. Fine metallic particles form in an insulating matrix if the volume fraction of metal is sufficiently small and if the constituents have no mutual solubility. Short range diffusion of the condensed atoms is a prerequisite, which may demand elevated substrate temperatures. In this type of coatings the metal grains are stabilized by the surrounding matrix, and also heat conduction across the film is easier than for gas evaporated specimens. The main disadvantage lies in the complex fabrication technique, which is not readily applicable to very large areas. Below we discuss coevaporated Co-Al₂O₃ /40/ cermets and cosputtered Au-MgO /41 - 43/ and Cr-Cr₂O₃ /44/ cermets.

We prepared Co-Al₂O₃ films by dual beam evaporation from two electron guns in a diffusion pumped vacuum system. The composition was determined via rate control with programmable quartz crystal oscillators to regulate the gun power. Figure 16 depicts a typical transmission electron micrograph for a cermet containing approximately 20 vol. % Co. Well separated rounded particles are found. Similar micrographs have been published for coevaporated Ni-Al₂O₃ films by Craighead and Buhrman /4/. Our films were deposited onto transparent substrates as well as onto glass plates covered with opaque silver layers. Spectral reflectance for cermet films with different metal contents on Ag backings are shown in figure 17. Film thicknesses lie in the range 55 to 68 nm. The data exhibit a spectral selectivity which becomes more pronounced for the higher metal concentrations. Recently we have determined optical constants for Co-Al₂O₃ cermets by a novel technique /45/ which combines transmittance data for films on transparent substrates with reflectance data for identical films backed by metal. These results, which will be presented elsewhere /40/, permit a more detailed comparison with theories than experimental recordings of either spectral transmittance or spectral reflectance.

Cermets consisting of cosputtered Au-MgO have been studied by Fan and Zavracky /41/ and also by Gittleman et al. /42/. They found that such films, deposited onto molybdenum-coated stainless steel, could display a solar absorptance exceeding 0.9 and a thermal emittance around 0.1. These observations, together with the reported stability up to 400°C, make these gold cermets very interesting for photothermal conversion of solar energy. The solid curves and the filled circles in figure 18 represent experimental results for the dielectric permeability $\bar{\epsilon} \equiv \bar{\epsilon}_1 + i\bar{\epsilon}_2$

of MgO + 25 vol. % Au.

Co-Al₂O₃ cermet

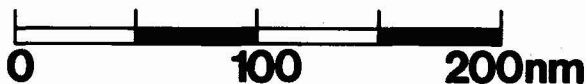
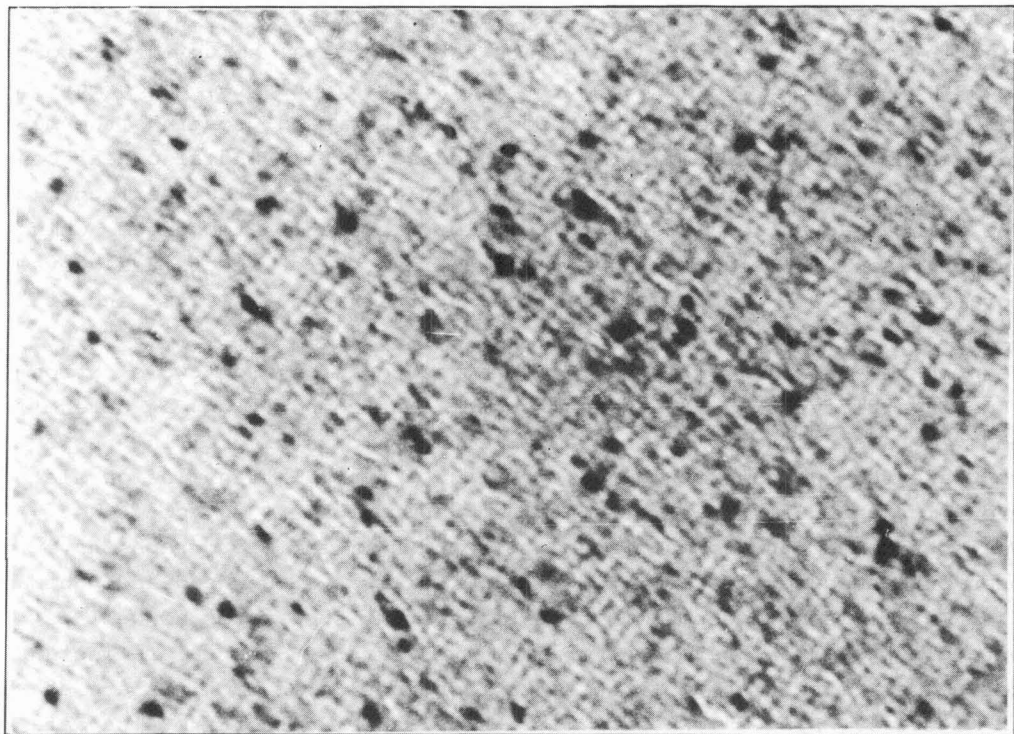


Fig.16.- Transmission electron micrograph for a coevaporated Co-Al₂O₃ cermet film.

These data are compared /43/ with computations employing the Maxwell Garnett theory as well as the Bruggeman theory ; both formalisms are considered since the microstructure of the cermets is not known. The variously dashed and dotted graphs pertain to different mean free paths of the conduction electrons. The curves for $\ell = 0.5$ nm show a remarkably good agreement with the measurements when the Bruggeman theory is used, whereas none of the theoretical curves display such correspondence for the Maxwell Garnett theory. A short mean free path is indeed ex-

pected for codeposited films, since the metallic particles are likely to contain large amounts of defects. We take the results of figure 18 as evidence that the microstructure of Au-MgO cermets is such that the Bruggeman theory is valid. This conclusion is supported by recent work reported by Buhrman and Craighead /46/.

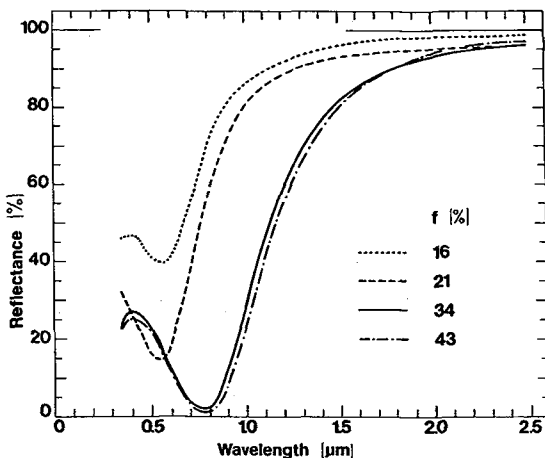


Fig.17.- Spectral reflectance for coevaporated $\text{Co-Al}_2\text{O}_3$ cermet films on Ag. Data are shown for four different volume fractions of Co.

MgO + 25%Au MAXWELL GARNETT THEORY

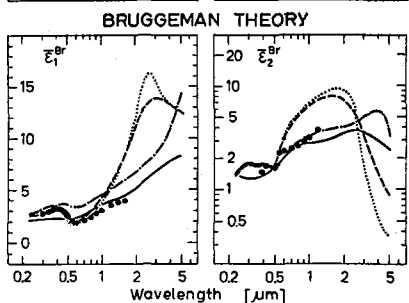
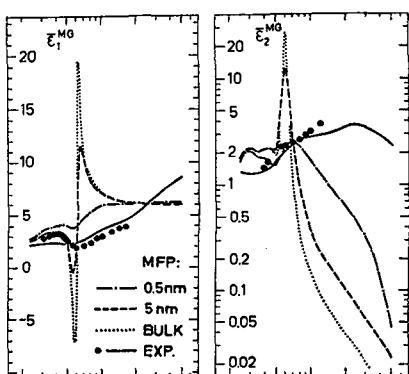


Fig.18.- Solid curves and filled circles denote experimental data for cosputtered Au-MgO cermets as obtained from references /41, 42/. Dashed and dotted curves represent calculations based on the Maxwell Garnett and Bruggeman effective medium theories with three different values of the electron mean free path (MFP).

However, other cermets, such as coevaporated $\text{Ni-Al}_2\text{O}_3$ /4/ and cosputtered W-MgO /42/, follow predictions from the Maxwell Garnett theory accurately, so for these cases it appears that the microstructure can be described as particles in a continuous host.

Another very interesting cermet is cosputtered $\text{Cr-Cr}_2\text{O}_3$, which has been investigated by Fan /44/. Figure 19 shows experimental data for real and imaginary parts of the dielectric permeability for cermets with three different amounts of Cr. These results are compared with computations based on the two effective medium theories.

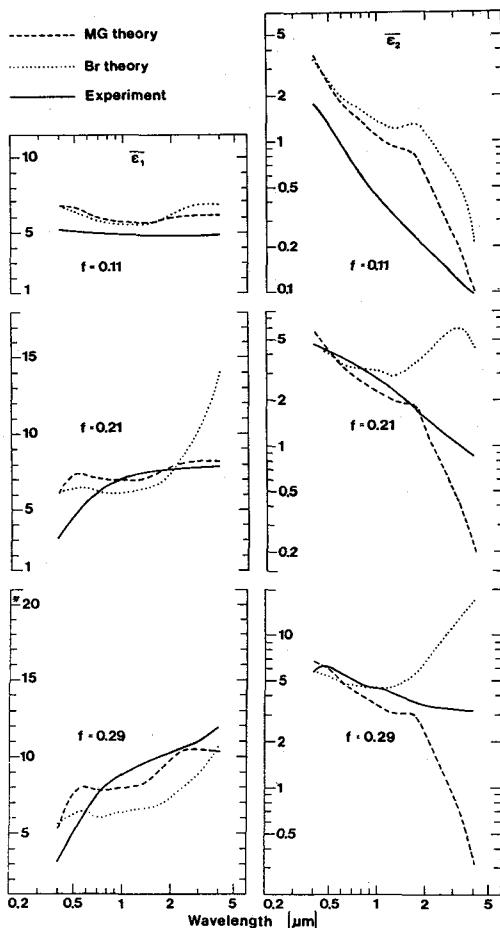


Fig.19.- Solid curves show experimental data for cosputtered $\text{Cr-Cr}_2\text{O}_3$ cermets as obtained from reference 44. Dashed and dotted curves represent calculations based on the Maxwell Garnett and Bruggeman effective medium theories.

The correspondence between theory and experiments is rather unsatisfactory. The systematic discrepancy for $f = 0.11$, where the measured data lie below the computed curves for both theories, might be blamed on an inaccuracy in the determination of metal content, but such an explanation is certainly insufficient for the other specimens. Looking at the

data for $\bar{\epsilon}_2$, it appears that the experimental curves lie in between the predictions from the two theories. It is worth noticing that Fan /44/ concluded from a comparison with the Maxwell Garnett theory, that "up to 30 vol. % the measured and predicted values match quite well". We feel that this statement is misleading. It is apparently based on the fact that Fan made his comparison at $\lambda = 2 \mu\text{m}$ only. At this particular wavelength the Maxwell Garnett theory is indeed in quite good agreement with the recorded $\bar{\epsilon}_1$ and $\bar{\epsilon}_2$ values, but the correspondence is far less convincing for other wavelengths. This points at the important fact that comparisons with theory should not be restricted to just a few wavelengths but should be extended over as wide an interval as possible. The theoretical understanding of the codeposited cermets is thus somewhat fragmentary. It seems that the microstructure topology plays a crucial role, which calls for careful sample analysis. Further complication occurs as a result of the great impurity of the constituent materials and the irregular grain shapes.

6. Electrodeposited films.— Electrodeposited black chrome is presently the most widely used coating for practical absorber surfaces. The solid curves in figure 20 show spectral reflectance from three different studies /47 - 49/.

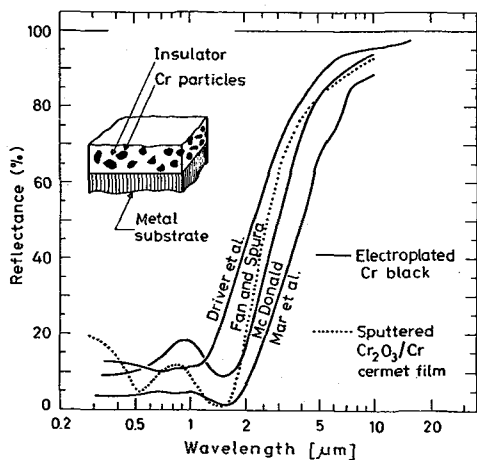


Fig.20.— Spectral reflectance for three films of electrodeposited black chrome (Refs. /47,49/) and one film of cosputtered Cr-Cr₂O₃ (Ref. /44/).

The good spectral selectivity, together with the good durability, motivates the widespread use. The microstructure of this type of coatings has only recently become firmly established as a result of electron microscopy /50 - 53/, which has proved that a granular configuration with metallic Cr particles embedded in insulating Cr₂O₃ is appropriate. This

structure is sketched in the inset of figure 20. It is therefore meaningful to compare the results for electrodeposited coatings with those for codeposited cermets. The dotted curve in figure 20 refers to the work by Fan and Spura /44/ ; it is found to be in good agreement with the solid curves.

Model calculations pertaining to the Cr-Cr₂O₃ structure has been presented in several papers /18, 44, 52 - 55/. These yield a spectral selectivity which resembles the measured one. However, a final comparison of theory and experiments can be performed only when the characterization of the electrodeposited coatings has advanced considerably beyond its present level.

7. Coloured anodic aluminium oxide films.- Anodic Al₂O₃ films can be coloured by several techniques /56/. The coatings are porous, which means that a conventional dyestuff pigment can be used. More lightfast colours can be obtained by electrolytic colouration, in which metallic particles are precipitated inside the pores /57, 60/. Metallic aluminium grains can be occluded in the oxide matrix by anodizing in special mixed acid electrolytes /33, 34/ ; this technique is known as integral colouration. Finally, colouration can be obtained also by anodization of Al-Si alloys. It is evident that several of the above types of coatings have the cermet structure. Below we discuss Ni pigmented Al₂O₃ produced by electrolytic colouration /7/ together with some results for integrally coloured films /61/.

Porous Al₂O₃ films were produced by dc-anodization of 99.5 % pure aluminium in dilute phosphoric acid. These translucent coatings were then blackened by ac electrolysis in a bath containing NiSO₄. The technique is known /57 - 60/ to yield metal precipitates inside the pores. The metal content could be varied by using different process parameters. The durability against excessive heating, humidity, and accelerated aging gave very satisfactory results /7/, indicating that Ni pigmented anodic Al₂O₃ films are sufficiently stable for use in practical photothermal converters of solar energy.

The coatings were analysed by several techniques. Scanning electron microscopy on fractured coatings, as seen from figure 21, showed inhomogeneous films with typical thicknesses of 0.7 µm. Auger electron spectroscopy combined with depth profiling by sputtering was used to analyse the cross-sectional composition of the films. Figure 22 proves that the nickel particles are confined to a layer near to the aluminium interface. A quantitative measure of the amount of Ni was obtained from atomic absorption analysis on dissolved coatings. Typical values lay

in the range $0.5 \leq \gamma \leq 1$ g Ni per m^2 anodized sheet. Our experimental characterization permits us to formulate the structural model shown in figure 23. The Al base metal is covered with a barrier layer of compact Al_2O_3 (denoted by 4), whose thickness /56/ is about 1 nm/V applied voltage during the anodization. This barrier is coated with $0.7 \mu\text{m}$ of porous Al_2O_3 . Its lowest portion (denoted by 3) is impregnated by metallic Ni. Typically, the Ni concentration is 0.23. The topmost layers consist solely of porous Al_2O_3 ; a division into two is motivated by an expected widening of the pores towards their openings. The table in the right hand part of figure 23 shows values of thickness t and expected surface roughness δt for the layers comprising a coating with $\gamma = 0.62 \text{ g/m}^2$. The table also contains some dielectric constants.

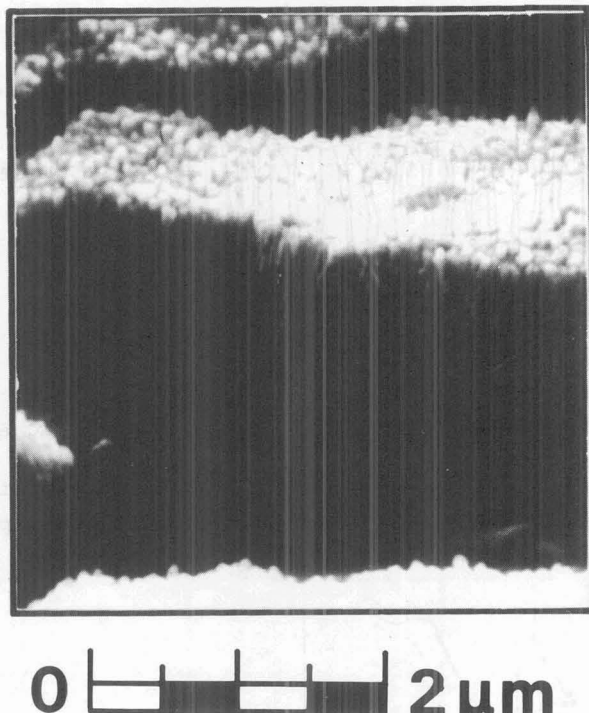


Fig.21.- Scanning electron micrograph of a fractured Ni pigmented anodic Al_2O_3 film.

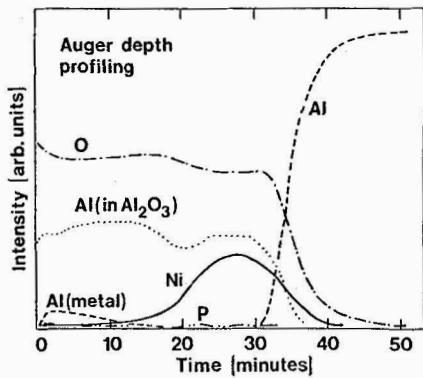


Fig.22.- Auger depth profiling data for a Ni pigmented anodic Al_2O_3 coating. The depth is proportional to a sputtering time.

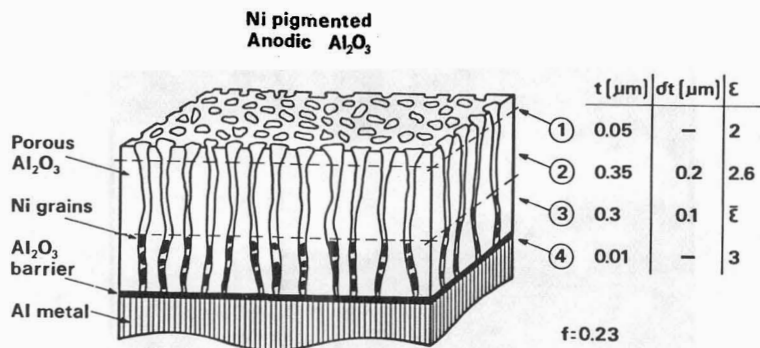


Fig.23.- Structural model for Ni pigmented anodic Al_2O_3 coatings.

Spectral reflectance data are shown in the main part of figure 24 for four anodic oxide coatings with different amounts of Ni pigment.

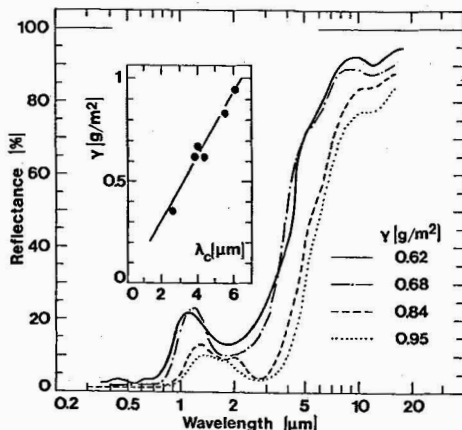


Fig.24.- Hemispherical spectral reflectance of Ni pigmented anodic Al_2O_3 coatings containing different amounts of Ni.

The wavelength corresponding to 50 % reflectance, λ_c , is found to lie in the interval $4 \leq \lambda_c \leq 6 \mu\text{m}$. Enhanced Ni content shifts λ_c towards longer wavelengths, as developed in the inset figure. Solar absorptance, a , and thermal emittance, $e(T)$, were evaluated by integrating the measured spectral reflectance curves over the solar spectrum AM2 and the Planck spectrum for $T = 65^\circ\text{C}$. Results are given in table IV.

Table IV.- Data for Ni pigmented anodic Al_2O_3 coatings.

$[\gamma/\text{m}^2]$	a	$e(65^\circ\text{C})$
0.62	0.92	0.10
0.68	0.93	0.13
0.84	0.96	0.20
0.95	0.97	0.26

The optical properties of the Ni pigmented layer in the structural model were computed by use of the Maxwell Garnett and Bruggeman theories. Both formalisms were used since the microstructure topology is not known. These data were then used in a matrix formulation /62/ of Fresnel's equations to compute the reflectance of the four-layer stack. The optical constants of Ni were taken from the literature /39, 63, 64/. The significance of the individual layers in the structural model is developed in figure 25. The reflectance of the bare Al surface is seen to exceed 85 % irrespective of wavelength. Application of the pigmented layer taken to contain spherical grains (layer 3) is seen to yield a selectivity which resembles the measured one provided that the Bruggeman effective medium theory is used, whereas the Maxwell Garnett theory is unable to give such agreement. Inclusion of the other layers, as seen from the solid curves, gives lowered reflectance at $\lambda \leq 3 \mu\text{m}$ and also introduces clear interference effects. These multiple peaks are to some extent artificial, though, since they require completely smooth surfaces, while real surfaces certainly exhibit irregularities. Assuming that the thickness variations are significant only over distances which are large compared with λ , and that every area element in the i^{th} film has equal probability of lying anywhere in the interval $t_i \pm \delta t_i/2$, is simple to include surface roughness in the computations. Figure 26 proves that with reasonable values of δt_2 and δt_3 only the main features of the interference peaks remain, which is in agreement with the experimental data.

The role of non-spherical particle shapes was investigated in a series of computations. The Ni particles were taken to be spheroidal with sym-

metry axis perpendicular to the film surface.

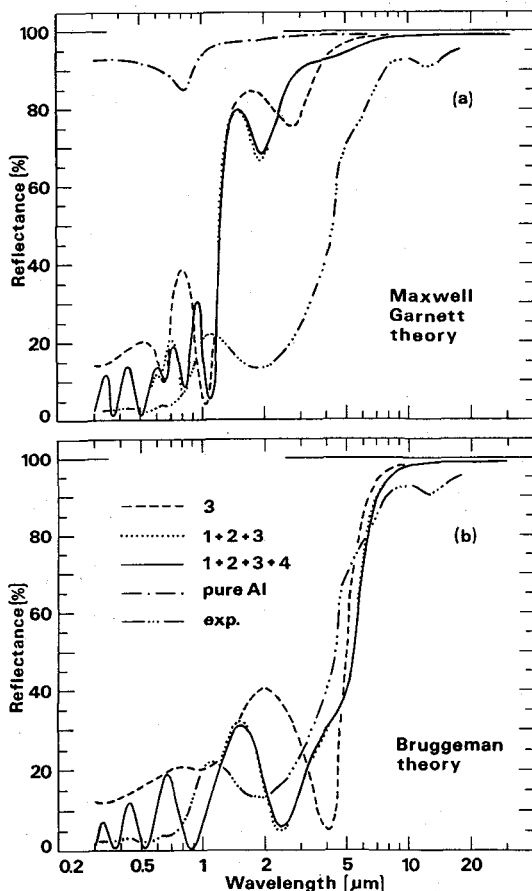


Fig. 25.- Computed and measured spectral reflectance for a Ni pigmented anodic Al_2O_3 film with $\gamma = 0.62 \text{ g/m}^2$. The numbers refer to the layers of the structural model (cf. Fig. 23).

This geometry makes it possible to characterize the shapes by one unique depolarization factor L . Figure 27 shows that for $L < 1/3$ (oblate spheroids) λ_c is shifted towards longer wavelengths, whereas for $L > 1/3$ (prolate spheroids) λ_c moves towards shorter wavelengths. In no case can a reasonable particle shape produce agreement between experiments and computations based on the Maxwell Garnett theory. It is clear from the data in figure 27 that a moderate elongation of the Ni particles in the direction of the pores improves the correspondence with experiments, provided that the Bruggeman theory is employed. Such an elongation is understandable from the structure of the anodized sheets and is also supported by electron microscopic evidence /58/. A final comparison of theory and experiments is given by figure 28, where the inset shows λ_c versus ratio between major and minor axes of prolate spheroidal particles. A value of $a/c \approx 1.24$ yields agreement to within $\sim 10\%$ over the

entire wavelength range, as seen from the main part of figure 28, where the Bruggeman theory was used.

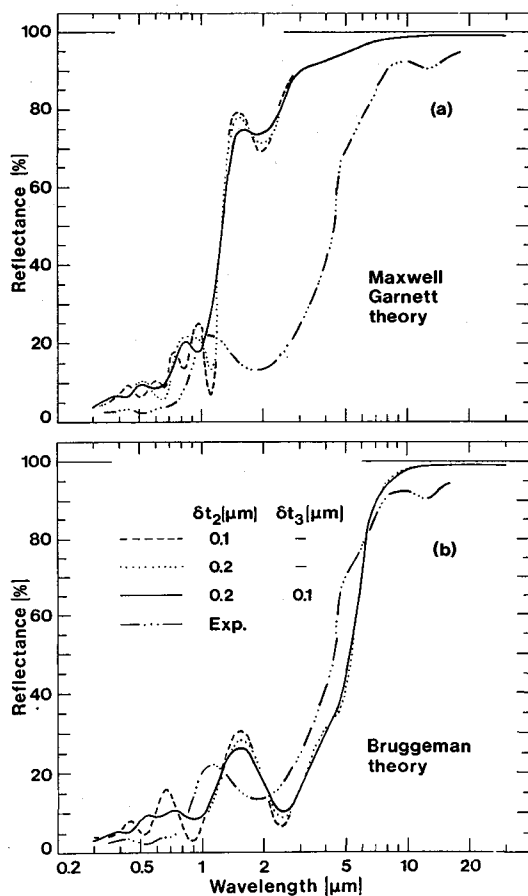


Fig.26.- Computed and measured spectral reflectance for a Ni pigmented anodic Al_2O_3 film with $\gamma = 0.62 \text{ g/m}^2$. Results are shown for different irregularities of layers 2 and 3.

It is of interest to study also integrally coloured anodic Al_2O_3 films which are known to be very lightfast and abrasion resistant /56/. They can be produced by anodizing in mixed acid electrolytes consisting of an organic acid, such as sulphosalicylic- or sulphophthalic acid, to which a small amount of sulphuric acid is added. It was shown by Wefers et al. /33, 34/ that such films are comprised of a dilute mixture of Al and Al_2O_3 . A similar structure can be produced also by immersion of Al sheet in dilute aqueous alkaline solutions containing silicate and borate salts and supersaturated with dissolved aluminium /35/. Such coatings have been produced for selective absorption of solar energy /65/. The filled circles in figure 29 show transmittance data /34/ at three wavelengths for this type of Al-Al₂O₃ cermets as a function of

volume fraction of Al.

Effective medium calculations encompassing two prescriptions for the mean free path are shown by the curves in figure 29. Since f is less than one percent, the Maxwell Garnett and Bruggeman theories give indistinguishable results. It is seen that good agreement is found between experiments and computations using the bulk mean free path. Summarizing, it is found that effective medium theories can be used to reproduce the optical properties of electrolytically and integrally coloured aluminium oxide. Some questions regarding microstructure topology and particle shape remain.

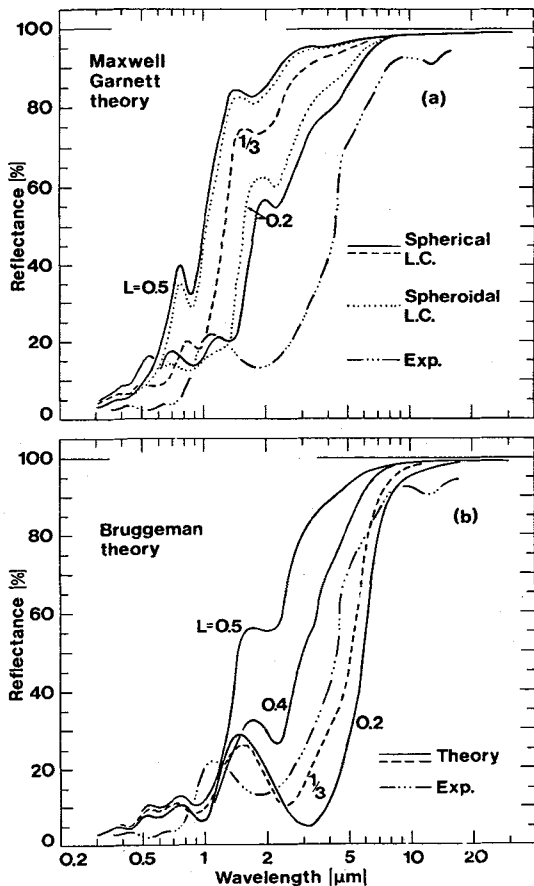


Fig. 27.- Computed and measured spectral reflectance for a Ni pigmented anodic Al_2O_3 film with $\gamma = 0.62 \text{ g/m}^2$. Results are shown for particles described by different depolarization factors.

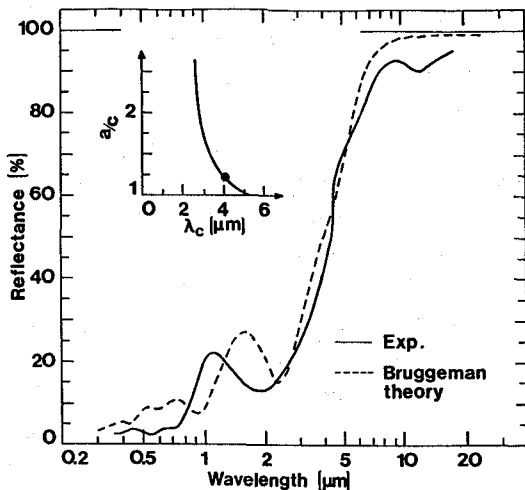


Fig.28.- Solid curve shows measured spectral reflectance for a Ni pigmented anodic Al_2O_3 film with $\gamma = 0.62 \text{ g/m}^2$. Dashed curve denotes computations using the Bruggeman theory for prolate spheroidal particles.

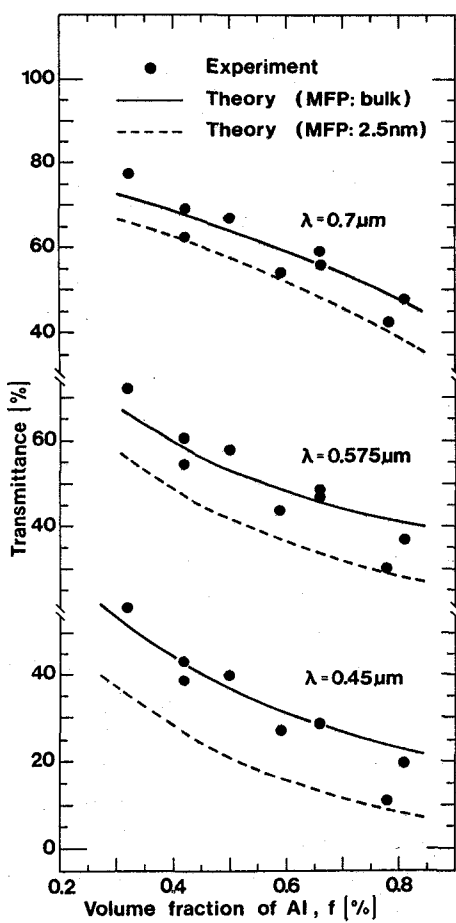


Fig.29.- Filled circles show measured transmittance for different wavelengths as reproduced from reference /34/. Curves denote effective medium calculations for two values of the electron mean free path (MFP).

8. Summary and remarks.- In this paper we have discussed several types of cermets. These materials are inhomogeneous and fine-grained, which makes it appropriate to treat their optical properties in terms of suitably averaged dielectric permeabilities. Two different averaging techniques must be employed depending on microstructure topology. The Maxwell Garnett theory is valid for particles embedded in a continuous host, whereas the Bruggeman theory holds for a random mixture of metallic and insulating spheres. These basic formulations can be derived by considering the scattering off properly defined random unit cells. Neither theory is limited to very small concentrations. By an intuitive reasoning, the formulations can be extended to encompass size dependent electron scattering, shape and orientation effects, and the role of certain types of local aggregations.

The theories are applied to several types of cermets. The optical transmittance through discontinuous films, being two-dimensional arrays of discrete islands, can be described by the Maxwell Garnett approach, if a thickness parameter is associated with the mean island - island separation. Gas evaporated coatings can also be understood from the Maxwell Garnett formalism, provided that the effect of local aggregates of particles is included semi-quantitatively. None of these cermets make practical absorbers - the single-layer discontinuous film has too low solar absorptance and the gas evaporated specimens are not mechanically stable. However, both are useful as models simulating the behaviour of more complex systems.

Codепosited films, prepared by evaporation or sputtering, can have microstructures such that either the Maxwell Garnett or the Bruggeman approaches are appropriate. It is likely that intermediate cases exist too. The theoretical understanding of these cermets is generally limited by a lack of proper sample characterization. Some electrodeposited layers may also be discussed in terms of effective medium theories, but for these the absence of detailed characterization is even more severe. In the last part of the paper we discussed coloured anodic aluminium oxide films. These materials have only rarely been considered together with other types of thin film cermets. However the metal pigmented anodic oxides have definitely cermet nature and their optical properties can be understood in some detail from effective medium theories. Furthermore, their excellent durability and the established industrial fabrication techniques make their optical and radiative properties worthy of more interest. Finally, it should be stressed that the above selection of cermets is by no means complete, but coatings made by chemical vapour deposition, ion implantation, and many more techniques, could have been added.

Acknowledgements.— Much of the work presented in this paper has been carried out in cooperation with O. Hunderi, Dept. of Physical Metallurgy, Norwegian Institute of Technology, Trondheim, Norway, and with G.A. Niklasson, Physics Dept., Chalmers University of Technology. The work on discontinuous gold films was performed together with S. Norrman and T. Andersson at Chalmers University. The study of Ni pigmented anodic Al_2O_3 was performed together with Å. Andersson, Gränges Aluminium, Fingång, Sweden. Helpful comments on the manuscript were given by A. Hjortsberg, O. Hunderi, and G.A. Niklasson.

References

- /1/ Sievers, A.J., in Solar Energy Conversion : Solid-State Physics Aspects, edited by B.O. Seraphin, Topics in Applied Physics (Springer-Verlag, Berlin-Heidelberg) 31, 1979, p. 57.
- /2/ Hahn, R.E. and Seraphin, B.O., in Physics of Thin Films, edited by G. Hass and M.H. Francombe (Academic Press, New York) 10, 1978, p.1.
- /3/ Seraphin, B.O., in Solar Energy Conversion : Solid-State Physics Aspects, edited by B.O. Seraphin, Topics in Applied Physics (Springer-Verlag, Berlin-Heidelberg) 31, 1979, p.5.
- /4/ Craighead, H.G. and Buhrman, R.A., Appl. Phys. Lett. 31 (1977) 423 ; J. Vac. Sci. Technol. 15 (1978) 269 ; Craighead, H.G., Bartynski, R., Buhrman, R.A., Wojcik, L. and Sievers, A., Sol. Energy Mater. 1 (1979) 105.
- /5/ Bastien, R.C., Austin, R.R. and Pottenger, T.P., Proc. Soc. Photo-Opt. Instrum. Eng. 140 (1978) 140.
- /6/ Okuyama, M., Furusawa, K. and Hamakawa, Y., Sol. Energy 22 (1979) 479.
- /7/ Granqvist, C.G., Andersson, Å. and Hunderi, O., Appl. Phys. Lett. 35 (1979) 268 ; Andersson, Å., Hunderi, O. and Granqvist, C.G., J. Appl. Phys. 51 (1980) 754.
- /8/ Garnett, J.C.M., Philos. Trans. Roy. Soc. Lond. 203 (1904) 385 ; 205 (1906) 237.
- /9/ Bruggeman, D.A.G., Ann. Phys. Leipzig 24 (1935) 636.
- /10/ Smith, G.B., J. Phys. D10 (1977) L39.
- /11/ Lamb, W., Wood, D.M. and Ashcroft, N.W., AIP Conf. Proc. 40 (1978) 240.
- /12/ Smith, G.B., Appl. Phys. Lett. 35 (1979) 668.

- /13/ Elliott, R.J., Krumhansl, J.A. and Leath, P.L., Rev. Mod. Phys. 46 (1974) 465.
- /14/ Stroud, D. and Pan, F.P., Phys. Rev. B17 (1978) 1602.
- /15/ Euler, J., Z. Phys. 137 (1954) 318.
- /16/ Kreibig, U., Z. Phys. B31 (1978) 39.
- /17/ Granqvist, C.G. and Buhrman, R.A., J. Appl. Phys. 47 (1976) 2200.
- /18/ Granqvist, C.G. and Hunderi, O., J. Appl. Phys. 50 (1979) 1058
- /19/ Landau, L.D. and Lifshitz, E.M., Electrodynamics of Continuous Media (Pergamon, New York) 1960, p. 27.
- /20/ Fuchs, R., Phys. Rev. B11 (1975) 1732 ; Fuchs, R. and Liu, S.H., Phys. Rev. B14 (1976) 5521.
- /21/ Van de Hulst, H.C., Light Scattering by Small Particles (Wiley, New York) 1957.
- /22/ Bilboul, R.R., Brit. J. Appl. Phys. 2 (1969) 921.
- /23/ Donnadieu, A., Thin Solid Films 6 (1970) 249.
- /24/ Clippe, P., Evrard, R. and Lucas, A.A., Phys. Rev. B14 (1976) 1715.
- /25/ Granqvist, C.G. and Hunderi, O., Phys. Rev. B16 (1977) 3513.
- /26/ Zeller, H.R. and Kuse, D., J. Appl. Phys. 44 (1973) 2763.
- /27/ Norrman, S., Andersson, T., Granqvist, C.G. and Hunderi, O., Phys. Rev. B18 (1978) 674.
- /28/ Vlieger, J., Physica (Utrecht) 64 (1973) 63 ; Bedaux, D. and Vlieger, J., Physica (Utrecht) 67 (1973) 55; 73 (1974) 287.
- /29/ Winsemius, P., Ph.D. Thesis, Rijksuniversiteit te Leiden, the Netherlands (1973), unpublished.
- /30/ Granqvist, C.G. and Hunderi, O., Phys. Lett. 73A (1979) 213 ; J. Appl. Phys. 51 (1980) 1751.
- /31/ Granqvist, C.G. and Niklasson, G.A., J. Appl. Phys. 49 (1978) 3512.
- /32/ Niklasson, G.A. and Granqvist, C.G., J. Appl. Phys. 50 (1979) 5500.
- /33/ Wefers, K. and Evans, W.T., Plating and Surface Finishing 62 (1975) 951.
- /34/ Wefers, K. and Wallace, P.F., Aluminium (Düsseldorf) 52 (1976) 485.

- /35/ Cochran, W.C. and Powers, J.H., Aluminium (Düsseldorf) 54 (1978) 147.
- /36/ Mathewson, A.G. and Myers, H.P., Phys. Scr. 4 (1971) 291.
- /37/ Ashcroft, N.W. and Sturm, K., Phys. Rev. B3 (1971) 1869.
- /38/ Barker, A.S. and Ditzenberger, J.A., Phys. Rev. B1 (1970) 4378.
- /39/ Jonhson, P.B. and Christy, R.W., Phys. Rev. B9 (1974) 5056.
- /40/ Niklasson, G.A. and Granqvist, C.G., to be published.
- /41/ Fan, J.C.C. and Zavracky, P.M., Appl. Phys. Lett. 29 (1976) 478.
- /42/ Gittleman, J.I., Abeles, B., Zanzucchi, P. and Arie, Y., Thin Solid Films 45 (1977) 9.
- /43/ Granqvist, C.G., J. Appl. Phys. 50 (1979) 2916.
- /44/ Fan, J.C.C. and Spura, S.A., Appl. Phys. Lett. 30 (1977) 511 ; Fan, J.C.C., Thin Solid Films 54 (1978) 139.
- /45/ Hjortsberg, A., Thin Solid Films 69(1980)L15;Appl.Opt., to be published.
- /46/ Buhrman, R.A. and Craighead, H.G., in Topical Meeting on Optical Phenomena Peculiar to Matter of Small Dimensions (Tucson, Arizona, USA) 1980 ; paper ThA2 (unpublished).
- /47/ McDonald, G.E., Sol. Energy 17 (1975) 119.
- /48/ Mar, H.Y.B., Peterson, R.E. and Zimmmer, P.B., Thin Solid Films 39 (1976) 95.
- /49/ Driver, P.M., Jones, R.W., Riddiford, C.L. and Simpson, R.J., Sol. Energy 19 (1977) 301.
- /50/ Lampert, C.M. and Washburn, J.W., Sol. Energy Mater. 1 (1979) 81.
- /51/ Switkowski, Z.E., Heggie, J.C.P., Clark, G.J. and Petty, R.J., Australian J. Phys. 32 (1979) 343 ; Clark, G.J., Switkowski Z.E., Petty, R.J. and Heggie, J.C.P., J. Appl. Phys. 50 (1979) 4791.
- /52/ Ignatiev, A., O'Neill, P., Doland, C. and Zajac, G., Appl. Phys. Lett. 34 (1979) 42 ; Zajac, G. and Ignatiev, A., J. Vac. Sci. Technol. 16 (1979) 233 ; Ignatiev, A., O'Neill, P. and Zajac, G., Sol. Energy Mater. 1 (1979) 69.
- /53/ Berthier, S. and Lafait, J., J. Physique Paris 40 (1979) 1093.
- /54/ Hogg, S.W. and Smith, G.B., J. Phys. D. 10 (1977) 1863.
- /55/ Window, B., Ritchie, I.T. and Cathro, K., Appl. Opt. 17 (1978) 2637 ; Thin Solid Films 57 (1979) 309.

- /56/ Wernick, S. and Pinner, R., The Surface Treatment and Finishing of Aluminium, 4th edition (Robert Draper Ltd., Teddington, U.K.) 1972.
- /57/ Läser, L., Aluminium (Düsseldorf) 48 (1972) 169.
- /58/ Sandera, L., Aluminium (Düsseldorf) 49 (1973) 533.
- /59/ Sautter, W., Ibe, G. and Meier, J., Aluminium (Düsseldorf) 50 (1974) 143.
- /60/ Sheasby, P.G. and Cooke, W.E., Trans. Inst. Metal Finishing 52 (1974) 103.
- /61/ Granqvist, C.G., J. Appl. Phys. 51 (1980) 3359.
- /62/ Fowles, G.R., Introduction to Modern Optics (Holt, Rinehart, and Winston, New York) 1968.
- /63/ Kirillova, M.M., Zh. Eksperim. Teor. Fiz. 61 (1971) 336 [Sov. Phys. JETP 34 (1972) 178].
- /64/ Siddiqui, A.S. and Treherne, D.M., Infrared Physics 17 (1977) 33.
- /65/ Powers, J.H., Craig, Jr., A.G. and King, W., in Sharing the Sun : Solar Technology in the Seventies, Proc. Joint Conf. American Section ISES and SES of Canada (Winnipeg, Canada, 1976) edited by K.W. Böer, 6, p. 166.